# Incomplete fusion reactions for $^{19}F + ^{169}Tm$: Measurement of recoil range distributions

Mohd. Shuaib,[1,*] M. Shariq Asnain,[2] Aquib Siddique,[1] Ishfaq Majeed Bhat,[1] Manoj Kumar Sharma,[3] Abhishek Yadav,[4] Pushpendra P. Singh,[5] Devendra P. Singh,[6] R. Kumar,[7,†] B. P. Singh,[1,‡] and R. Prasad[1]

[1]*Department of Physics, Aligarh Muslim University, Aligarh 202 002, Uttar Pradesh, India*
[2]*School of Engineering Sciences and Technology, Jamia Hamdard, New Delhi 110062, India*
[3]*Department of Physics, University of Lucknow, Lucknow 226007, Uttar Pradesh, India*
[4]*Amity Institute of Nuclear Science and Technology, Amity University, Noida 201313, Uttar Pradesh, India*
[5]*Department of Physics, Indian Institute of Technology, Ropar 140 001, Punjab, India*
[6]*Department of Physics, University of Petroleum and Energy Studies, Dehradun 248 007, Uttarakhand, India*
[7]*Inter University Accelerator Centre, Aruna Asaf Ali Marg, New Delhi 110067, India*

(Received 7 July 2023; revised 30 April 2024; accepted 12 June 2024; published 22 July 2024; corrected 9 September 2024)

This present study explores the role of incomplete fusion in heavy-ion reactions alongside complete fusion, examining recoil ranges of populated residues. An attempt has been made to distinguish between complete and incomplete fusion contributions by analyzing linear momentum transfer from the projectile to the target nucleus. Employing the recoil-catcher activation technique, forward recoil range distributions for the $^{19}F + ^{169}Tm$ system at energies around 96 and 106 MeV have been measured. Analysis of these recoil range distributions reveals characteristics of complete and incomplete fusion processes. Complete fusion reactions show larger recoil ranges, signifying comprehensive linear momentum transfer. On the other hand, residues exhibiting smaller recoil ranges result from partial linear momentum transfer due to incomplete fusion of the projectile. The forward recoil range distributions indicate an admixture of full and partial linear momentum transfer components in reactions with $\alpha$ particles in the exit channels. This behavior suggests projectile breakup caused by the Coulomb effect, offering valuable insights into fusion process dynamics.

DOI: 10.1103/PhysRevC.110.014621

## I. INTRODUCTION

Since the early 2010s, significant progress has been achieved in understanding the dynamics of heavy-ion- (HI) induced fusion reactions, owing to their pivotal role in generating and studying exotic nuclei [1–7]. When two heavy nuclei fuse together, a relatively massive nucleus is formed, which can subsequently undergo fission and/or quasifission [8–11]. Despite this, a notable reduction in fusion cross sections has been observed in HI reactions due to projectile breakup [12–18]. Consequently, it is imperative to thoroughly investigate HI fusion reactions to comprehend the impact of breakup on the fusion process. Several studies [12–19] have reported the observation of incomplete fusion (ICF) reactions, wherein the projectile fragments on collision at energies slightly above the Coulomb barrier. This projectile breakup leads to a significant suppression of the complete fusion (CF) cross section, both for weakly and strongly bound projectiles [12–19]. This suppression is closely linked to the breakup threshold energy of the projectile in ICF reactions [20–25]. Therefore, at low energies, both CF and breakup fusion reactions dominate and compete with each other [20–31].

In the CF process, the entire projectile merges with the target nucleus with all possible partial waves $\ell$ below a critical value $\ell_{crit}$. As per the sharp cut-off approximation [31–33], the $\ell_{crit}$ is defined as the angular momentum value at which the attractive pocket in the potential energy plot is retained, allowing for the fusion of the entire projectile. This process leads to the formation of a composite system with predetermined mass, charge, and excitation energy. In contrast, the ICF process hinders the complete fusion of the entire projectile, allowing partial waves with $\ell > \ell_{crit}$ to contribute to the formation of an incompletely fused compound nucleus. Consequently, during an inelastic interaction, the projectile may break up, and one of the fragments can still fuse with the target nucleus. The unfused fragment of the projectile continues moving forward with nearly the same velocity as the incident beam. The compound nucleus formed in this ICF process has a lower charge, mass, and excitation energy compared to that formed in CF. Figure 1 illustrates a representative case of HI interactions resulting in various reaction processes.

Several models [32,34,35] have been proposed to analyze the reaction dynamics of the ICF process. The SUMRULE model [32,34] is based on the partial statistical equilibrium and a generalized concept of critical angular momentum. It suggests that mass transfer can occur if the relative angular momentum of the captured fragment concerning the target nucleus is smaller than the $\ell_{crit}$ for the incompletely fused system. This implies that ICF primarily occupies the $\ell$ space

*Contact author: shuaibphy67@gmail.com
†Deceased.
‡Contact author: bpsinghamu@gmail.com

 

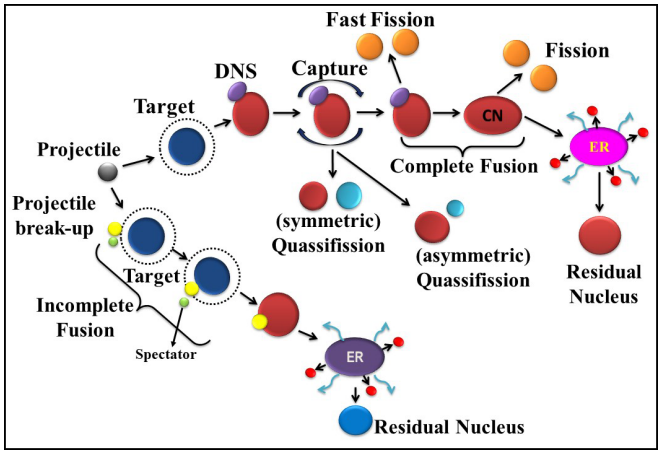


FIG. 1. A typical description of HI interactions indicating some of the possible decay modes.

above $\ell_{\rm crit}$ for CF. Yadav *et al.* [36], recently attempted to ascertain the magnitude of the ICF process for the $^{12}C + ^{159}Tb$ system using the parameters outlined in Ref. [32]. However, the SUMRULE model was found to significantly underestimate the ICF reaction cross section for the relevant residues. Parker *et al.* also noted similar deviations for the $^{12}C + ^{51}V$ system at energies up to 100 MeV [30,37]. On the other hand, the Hot spot model [35] exclusively offers insights into the characteristics of the spectrum of the light-projectile-like pre-equilibrium component. These previously mentioned models have typically been employed to fit experimental data obtained at energies $E \geqslant 10$ MeV/nucleon or higher. However, there has been no satisfactory explanation for ICF data at low energies (i.e., ≈4–7 MeV/nucleon). Consequently, the study of ICF reactions remains an active area of investigation due to the absence of any reliable theoretical model or systematics.

In a recent study, Diaz-Torres *et al.* [38] proposed a three-dimensional classical model for low-energy ICF reactions. This model exhibited promise in accurately reproducing both CF and ICF cross sections. However, its applicability was confined to light-ion beams with a relatively low break-up threshold energy. Consequently, a comprehensive understanding of ICF reactions at low energies requires further investigation, given the limited availability of theoretical models. Notably, most reported ICF studies have employed HI clustered beams such as $^{12}C$, $^{16}O$, and $^{20}Ne$ [39–42]. These beams play a crucial role in HI reactions, especially in exploring the dynamics of the ICF process concerning projectile break-up into $\alpha$-clustered fragments. Each $\alpha$-fragment can significantly contribute to the ICF process. Nevertheless, it would be intriguing to conduct more measurements on break-up reactions using an HI beam like $^{19}F$.

A few studies are available on the cluster structure of the $^{19}F$ projectile ($N \neq Z$), with the aim of identifying $\alpha$ and other more exotic structures [43,44]. It has been observed that the exotic cluster configurations in these systems exhibit structures reminiscent of chemical bonding. The excited levels in $^{19}F$ have been analyzed using more sophisticated models [45,46]. It is important to note that $^{19}F$ is a one-proton deficient system of $^{19}Ne$, and its level sequence is interpreted by considering the $\alpha$-hole cluster model, as well as the coupling of the $\alpha + ^{15}N$ and $t + ^{16}O$ channels [45,46]. The study of $\alpha + ^{15}N$ has been reported in Ref. [47]. The breakup of $^{19}F$ into the fragments may be considered as a result of ICF only, as the probability of deep inelastic collision at these energies is less likely [33]. Consequently, a comprehensive experimental study of break-up fusion reactions at low energies with a $^{19}F$ beam is necessary to obtain a complete description. Thus, investigating the role of projectile structure in the dynamics of the break-up fusion process becomes imperative.

In the present work, we have studied different linear momentum transfer (LMT) components involved in breakup reactions through recoil range distributions (RRDs) for the $^{19}F + ^{169}Tm$ system at energies of 96 and 106 MeV. The relative contributions of CF and ICF processes have already been determined by analyzing the experimental excitation functions (EFs) of reaction residues in the energy range of ≈4–7 MeV/nucleon [25] and with the statistical model code PACE4 [48], offering a model-dependent approach to data analysis. However, from a physics perspective, a model-independent approach is preferred to clearly indicate the existence of such reactions at low energies. To address this, we adopted a model-independent approach by extracting the relative contribution of CF and ICF events through evaluating the degree of linear momentum transfer ($\rho_{\rm LMT}$) from the projectile to the target nucleus. This is done by measuring the RRDs of the reaction residues in the exit channels. By employing this model-independent and irrefutable approach, a pivotal aspect of the paper is provided. Through this method, we can gain a more comprehensive and better understanding of the contributions of both CF and ICF processes in the experimental observations. This approach allows us to assess the relative importance of each process based on the degree of linear momentum transfer, providing valuable insights into the intricate dynamics of the investigated reaction.

This current investigation constitutes a vital addition to the available data, providing supplementary insights into the breakup process in HI reactions involving a $^{19}F$ beam. The significance of this study lies in its departure from the predominant focus of previous studies, which has predominantly concentrated on the measurement and analysis of EFs for this specific system [25]. The paper is structured as follows: Section II presents the experimental details regarding recoil range distribution measurements, Sec. III focuses on the analysis and interpretation of the data, and Sec. IV encapsulates the summary and conclusions of the work.

## II. EXPERIMENTAL DETAILS

The RRD experiments aimed at distinguishing between CF and/or ICF events involved a $^{19}F$ beam directed at a $^{169}Tm$ target. The $^{19}F$ beam was obtained from the 15UD pelletron at the Inter University Accelerator Center (IUAC) in New Delhi, India. The RRD measurement setup comprised of a thin target of $^{169}Tm$ with a thickness of ≈169 μg/cm$^2$ (with nearly 100% abundance and deposited on a thin aluminum backing). This was followed by a series of extremely thin aluminum catcher foils with thicknesses ranging from ≈10–80 μg/cm$^2$). Two stacks, each consisting of a series of these thin aluminum

TABLE I. Thickness of aluminium catcher foils used to trap the recoiling residues at 96- and 106-MeV beam energy.

| $E_{lab} \approx 96$ MeV | | | $E_{lab} \approx 106$ MeV | | |
|---|---|---|---|---|---|
| Catcher No. | Thickness ($\mu g/cm^2$) | CT[a] ($\mu g/cm^2$) | Catcher No. | Thickness ($\mu g/cm^2$) | CT[a] ($\mu g/cm^2$) |
| C1 | 38.2 | 38.2 | E1 | 15.4 | 15.4 |
| C2 | 42.0 | 80.2 | E2 | 35.5 | 50.9 |
| C3 | 43.2 | 123.4 | E3 | 36.8 | 87.7 |
| C4 | 43.4 | 166.8 | E4 | 37.9 | 125.6 |
| C5 | 43.5 | 210.3 | E5 | 38.1 | 163.7 |
| C6 | 44.1 | 254.4 | E6 | 38.2 | 201.9 |
| C7 | 44.2 | 298.6 | E7 | 38.1 | 240.0 |
| C8 | 45.4 | 344.0 | E8 | 38.3 | 278.3 |
| C9 | 47.2 | 391.2 | E9 | 39.4 | 317.7 |
| C10 | 48.0 | 439.2 | E10 | 39.5 | 357.2 |
| C11 | 49.5 | 488.7 | E11 | 40.0 | 397.2 |
| C12 | 50.5 | 539.2 | E12 | 40.5 | 437.7 |
| C13 | 50.5 | 589.7 | E13 | 41.7 | 479.4 |
| C14 | 50.5 | 640.2 | E14 | 43.0 | 522.4 |
| C15 | 50.6 | 690.8 | E15 | 45.4 | 567.8 |
| C16 | 53.0 | 743.8 | E16 | 45.8 | 613.6 |
| C17 | 53.0 | 796.8 | E17 | 49.5 | 663.1 |
| C18 | 89.8 | 886.6 | E18 | 50.5 | 713.6 |
| C19 | 90.3 | 976.9 | E19 | 51.8 | 765.4 |
| C20 | 94.9 | 1071.8 | E20 | 57.1 | 823.1 |

[a]CT: cumulative thickness.

catcher foils, were irradiated at distinct beam energies of ≈96 and 106 MeV, respectively. The thicknesses of the catcher foils used to trap the recoiling residues are detailed in Table I. The catcher foils were affixed to steel holders of thickness 0.5 mm. Figure 2 shows a typical arrangement of the stack, with the $^{169}$Tm target followed by the series of thin aluminum catcher foils, mounted inside the scattering chamber. The use of several thin catcher foils provides better resolution and enables the trapping of recoiling residues produced through different LMT events, namely CF and/or ICF processes. The thickness of the target and each aluminum catcher foil was predetermined using the $\alpha$-transmission technique. Irradiations were carried out at both energies for approximately 14 h each in the 1.5-m General Purpose Scattering Chamber (GPSC) [49], equipped with an In-vacuum Transfer Facility (ITF). The ITF technique minimizes the time gap between the end of irradiation and the start of sample counting. This allows for the removal of samples from the GPSC within 4–5 min of the irradiation stop time, without breaking the vacuum, enabling the prompt counting of short-lived activities. The decrease in beam energy of $^{19}$F at half thickness was determined using the stopping power and range code SRIM [50].

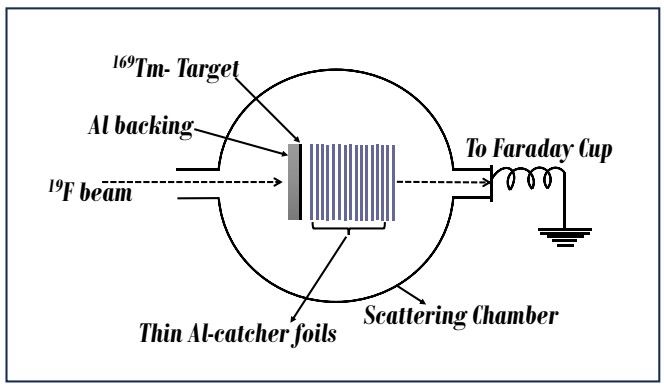


FIG. 2. A typical stack arrangement consisting of $^{169}$Tm target followed by a series of thin Al-catcher foils.

The incident beam had an energy of 96 MeV with a 500-keV energy spread. The beam current remained at about 5 pnA, and the Faraday cup downstream determined the beam flux by measuring the total charge collected in the catcher stack. Radioactivities induced in each catcher foil were measured using a high-resolution HPGe spectrometer coupled to the CANDLE data acquisition system [51]. The High Purity Germanium (HPGe) spectrometer had a 2-keV energy resolution for the 1.33-MeV $\gamma$-ray emission from a $^{60}$Co radioactive source. The recoiling heavy residues traveled approximately 10 mm through the catcher stack, resulting in a time-of-flight (TOF) of a few nanoseconds. This TOF was much shorter than the half-lives of the residues, minimizing significant decay effects during TOF. After irradiation, the catcher foil stack was removed, and the induced activities in each catcher foil were individually measured using the HPGe detector counting setup. Each catcher foil was measured individually, eliminating expected contamination from neighboring catchers. Lead shielding was used to reduce background radiation, and standard sources like $^{60}$Co, $^{133}$Ba, $^{137}$Cs, and $^{152}$Eu were employed for energy and efficiency calibrations of the HPGe $\gamma$-ray spectrometer.

The reaction residues were identified based on their characteristic $\gamma$-ray emissions in the spectrum and were further confirmed through their decay curves. For the decay curve

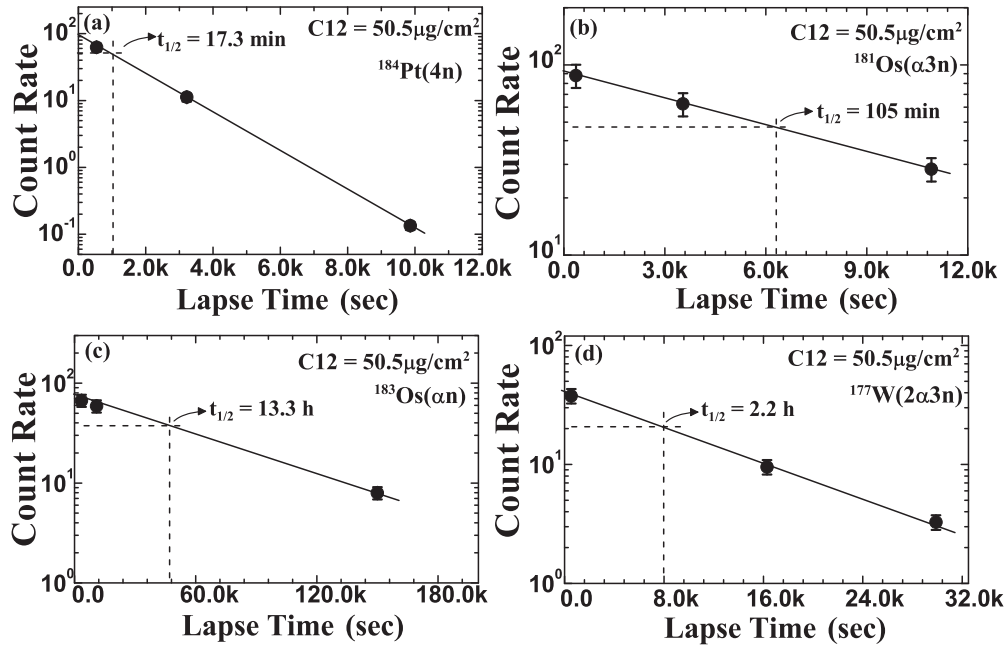


FIG. 3. The decay curves of residues (a) $^{184}$Pt ($t_{1/2} = 17.3$ min), (b) $^{181}$Os ($t_{1/2} = 105$ min), (c) $^{183}$Os ($t_{1/2} = 13$ h), and (d) $^{177}$W ($t_{1/2} = 2.2$ h) at cumulative thickness ≈539.2 μg/cm$^2$ (C12).

analysis, each sample was counted multiple times to obtain accurate measurements of the half-lives of the identified residues. Figures 3(a)–3(d) illustrates the half-lives ($t_{1/2}$) of four reaction residues: $^{184}$Pt (with $t_{1/2} = 17.3$ min), $^{181}$Os ($t_{1/2} = 105$ min), $^{183}$Os ($t_{1/2} = 13$ h), and $^{177}$W ($t_{1/2} = 2.2$ h) as representative cases. These residues exhibit a range of different lifetimes. As shown in Figs. 3(a)–3(d), the measured half-lives for each residue are in good agreement with the values reported in the literature [52,53]. Figures 4(a)–4(c), displays the $\gamma$ spectra recorded at different catcher foils E5, E10, and E15 at an incident energy of 106 MeV. The spectrum includes the $\gamma$ rays of interest. Background spectra were recorded before and after the experiment, and the subtraction of the background from the recorded spectra was performed using the CANDLE software [51]. The identification of reaction residues and their respective spectroscopic properties is obtained from the Table of Isotopes [52] and Wallet Card [53]. The decay data and spectroscopic properties of the identified reaction residues are presented in a tabulated format in Table II. The intensity of characteristics $\gamma$ lines has been used to determine the cross section of respective reaction residues. A standard formulation [40] based on FORTRAN program exp-sigma has been used to determine the cross section given by the equation

$$\sigma_r = \frac{A\lambda\exp(\lambda t_2)}{N_0\phi\theta G_\epsilon K[1-\exp(-\lambda t_1)][1-\exp(-\lambda t_2)]}, \qquad (1)$$

where $\lambda$, $t_1$, $t_2$, and $t_3$ are the decay constant, stop time of irradiation, lapse time, and counting time. $N_0$ represents the initial nuclei count in the sample, $\theta$ is the branching ratio of the characteristic $\gamma$ rays, $\phi$ is the incident beam flux, $G_\epsilon$ is the geometry-dependent efficiency of the detector for a particular $\gamma$-ray energy, and $K = [1-\exp(\mu d)]/\mu d$ is the self-absorption correction factor for the material of the sample of thickness d (gm/cm$^2$) and of absorption coefficient $\mu$ (cm$^2$/gm). The factor $[1-\exp(\lambda t_1)]$ is the saturation correction factor and takes into account the decay of activity during irradiation. The cross section of the residues was measured in each catcher foil using the formulation mentioned in Eq. (1).

In the course of RRD measurements, the yields for specific residues can be influenced by errors and uncertainties, primarily stemming from counting statistics. Various factors contribute to the anticipated errors in the experimental yields. First, uncertainties may arise from fluctuations in the beam current, introducing variations in the intensity of the incident beam. Second, systematic uncertainties arise from detector calibration and the determination of geometry-dependent efficiency. The calibration procedures and calculations of the spectrometer's efficiency contribute to the overall

TABLE II. Relevant nuclear data of the reaction residues identified in the present work.

| Reactions | Residue | Half-life | $J^\pi$ | $E_\gamma$ (keV) | $I_\gamma$ (%) |
|---|---|---|---|---|---|
| $^{169}$Tm($^{19}$F, 4$n$) | $^{184}$Pt | 17.3 min | $0^+$ | 154.41 | 31 |
| $^{169}$Tm($^{19}$F, 5$n$) | $^{183}$Pt | 6.5 min | $1/2^-$ | 254.61 | 30 |
| $^{169}$Tm($^{19}$F, $p3n$) | $^{184}$Ir | 3.09 h | $5^-$ | 263.90 | 67.5[a] |
| $^{169}$Tm($^{19}$F, $p4n$) | $^{183}$Ir | 58 min | $5/2^-$ | 228.10 | 6.9 |
| $^{169}$Tm($^{19}$F, $\alpha n$) | $^{183}$Os | 13 h | $9/2^+$ | 381.76 | 77 |
| $^{169}$Tm($^{19}$F, $\alpha 3n$) | $^{181}$Os | 105 min | $1/2^-$ | 118.03 | 12.9 |
| $^{169}$Tm($^{19}$F, $\alpha 5n$) | $^{179}$Os | 6.5 min | $1/2^-$ | 165.6 | 34[a] |
| $^{169}$Tm($^{19}$F, $2\alpha 3n$) | $^{177}$W | 2.2 h | $0^+$ | 1036.4 | 10.3 |
| $^{169}$Tm($^{19}$F, $2\alpha p4n$) | $^{175}$Ta | 10.5 h | $7/2^+$ | 179.27 | 1.22 |

[a]These intensities are relative.

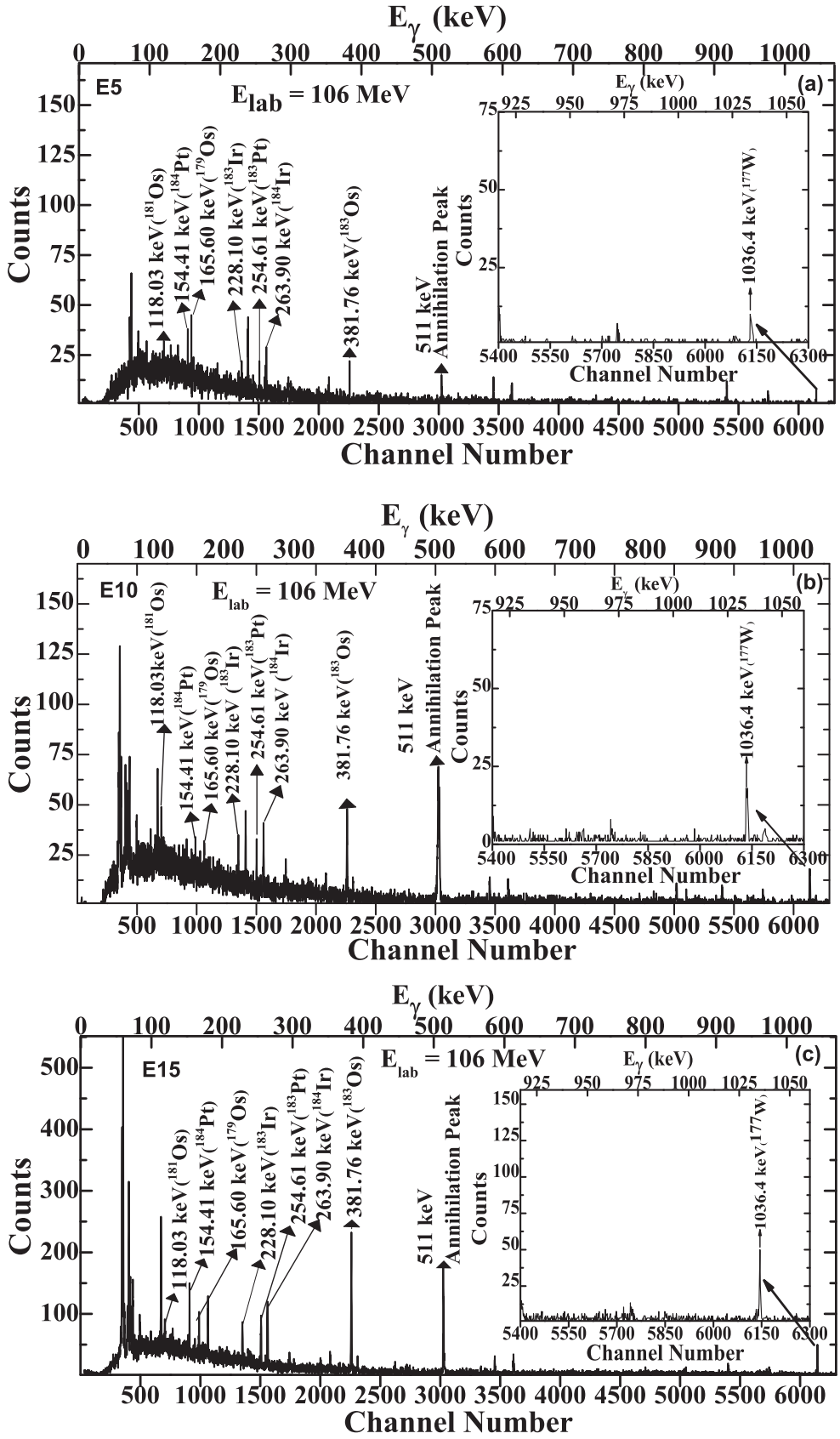


FIG. 4. [(a)–(c)] A typical singles $\gamma$ spectra recorded at different catcher foils E5, E10, and E15 respectively having cumulative thicknesses $\approx$163.7, 357.2, and 567.8 $\mu g/cm^2$ recorded at 106 MeV beam energy for $^{19}F + ^{169}Tm$ system. The inset figures represent the zoom version of $\gamma$ peak of energy $E_\gamma = 1036.4$ keV.

uncertainties in the measured yields. Additionally, uncertainties can arise from the Gaussian fitting of experimental data using ORIGIN software, as the fitting process introduces its own level of uncertainty. Considering these factors, along with the statistical error arising from counting statistics, the overall uncertainties in the measured yields are estimated to be less than 12%. It is important to note that this estimation encompasses the combined effect of all the mentioned factors. Furthermore, to determine the error in the most probable ranges, the expression $\sigma(\bar{x}) = \sigma/\sqrt{n}$ was utilized, where $\sigma$ represents the standard deviation. This calculation corresponds to the standard error of the mean. It is worth mentioning that the error depends on the number of samples, with a higher number of samples ($n$) resulting in a more precise estimate of $\bar{x}$ [54]. A detailed analysis of the recoil range distribution is provided in Sec. III.

## III. ANALYSIS AND INTERPRETATION OF DATA

Measuring how far the residues move in a stopping medium gives us information about momentum transfer and how reactions work. The degree of linear momentum transfer ($\rho_{\mathrm{LMT}}$) is determined by the ratio of $P_{\mathrm{frac}}$ (linear momentum of the fused part) to $P_{\mathrm{proj}}$ (initial momentum of the projectile). More $\rho_{\mathrm{LMT}}$ means higher recoil velocity ($v_o$) for reaction products, especially in CF. But in the case of ICF, the recoil velocity is lower because some linear momentum goes with the spectator. $\rho_{\mathrm{LMT}}$, linked to the fused mass of the projectile, gives max recoil velocity ($v_o$) for reaction products. Yet, in ICF, the recoil velocity is likely lower due to some linear momentum carried away by the spectator. As such, the RRD technique is quite a reliable method to disentangle apart different fusion processes (like CF and/or ICF) based on $\rho_{\mathrm{LMT}}$. This technique is able to separate out residues through different LMT components.

To determine the LMT involved in the reaction residues populated via specific channels such as $^{184}$Pt($4n$), $^{183}$Pt($5n$), $^{184}$Ir($p3n$), $^{183}$Ir($p4n$), $^{183}$Os($\alpha n$), $^{181}$Os($\alpha 3n$), $^{179}$Os($\alpha 5n$), $^{177}$W($2\alpha 3n$), and $^{175}$Ta($2\alpha p4n$), the normalized yield of the residues in each catcher foil is obtained by dividing its production cross section in the catcher by its respective thickness. The deduced yield for each catcher foil is plotted against the cumulative thickness. The experimental range distributions are then fitted with a Gaussian distribution function using the ORIGIN software [55]. As an example, the range distributions of $^{184}$Pt($4n$) residues at beam energies of approximately 96 and 106 MeV exhibit a single Gaussian peak, as shown in Figs. 5(a) and 5(b). From these figures, it can be observed that the most probable mean range ($R_P^{\mathrm{exp}}$) in the aluminum catchers is approximately 509 and 548 μg/cm$^2$ for projectile beam energies of 96 and 106 MeV, respectively. Furthermore, the experimentally deduced $R_P^{\mathrm{exp}}$ of $^{184}$Pt($4n$) residues from the range distribution is found to be in good agreement with the theoretically estimated mean range $R_P^{\mathrm{theo}}$ obtained using the SRIM code [50]. This confirms that only the full LMT component is involved in the population of $^{184}$Pt($4n$) residues at both studied energies.

Similar range distributions associated with the reaction channels $^{183}$Pt($5n$), $^{184}$Ir($p3n$), and $^{183}$Ir($p4n$) have also been observed, clearly indicating that these residues are populated as a result of complete momentum transfer, which is characteristic of the complete fusion process. However, in the case of $\alpha$-emitting channels, the range distributions of reaction residues, namely $^{183}$Os($\alpha n$), $^{181}$Os($\alpha 3n$), $^{179}$Os($\alpha 5n$), $^{177}$W($2\alpha 3n$), and $^{175}$Ta($2\alpha$p4n) have shown multiple Gaussian peaks. As an illustrative example, the range distributions for the $^{183}$Os($\alpha n$) residues at both energies 96 and 106 MeV are shown in Figs. 6(a) and 6(b), and can be deconvoluted into two Gaussian peaks at different cumulative depths, indicating the presence of more than one LMT component. In Fig. 6(a), the peak at the higher cumulative depth corresponds to the most probable range, $R_{\mathrm{exp}}^{p} = 539$ μg/cm$^2$ (Peak-I), while the peak at the lower depth corresponds to $R_{\mathrm{exp}}^{p} = 342$ μg/cm$^2$ (Peak-II). However, at energy $E_{\mathrm{lab}} = 106$ MeV, the most probable mean range $R_{\mathrm{exp}}^{p} = 363$ μg/cm$^2$ correspond to Peak-II, while $R_{\mathrm{exp}}^{p} = 550$ μg/cm$^2$ correspond to Peak-I. The difference in

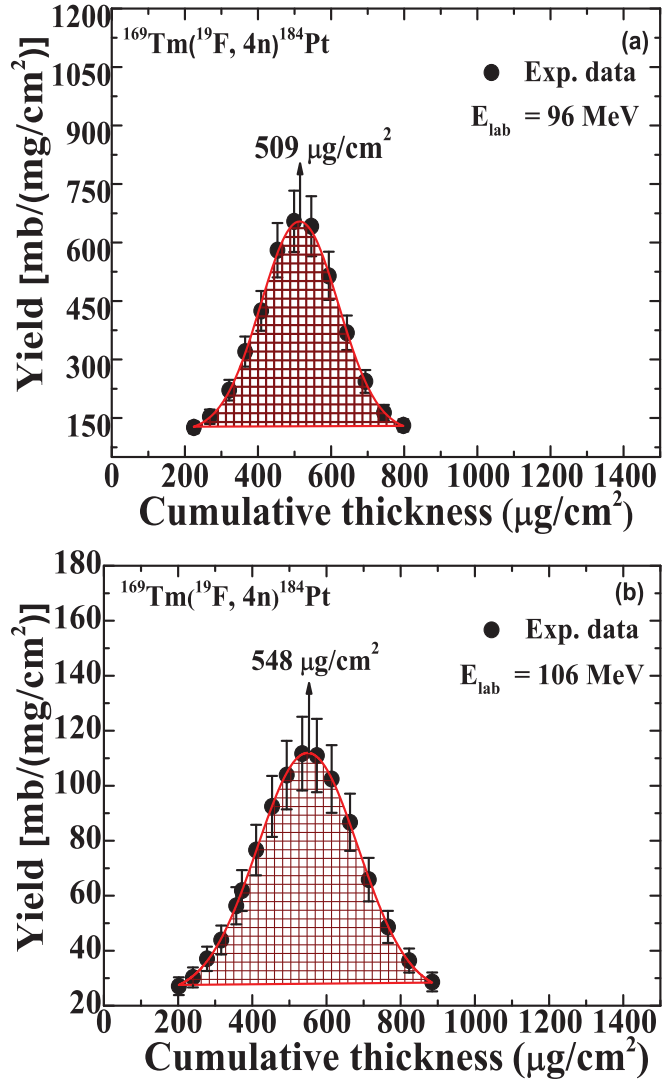


FIG. 5. [(a) and (b)] Experimentally measured recoil range distribution of $^{184}$Pt residues populated through $4n$ channel in $^{19}$F + $^{169}$Tm system at energies 96 and 106 MeV.

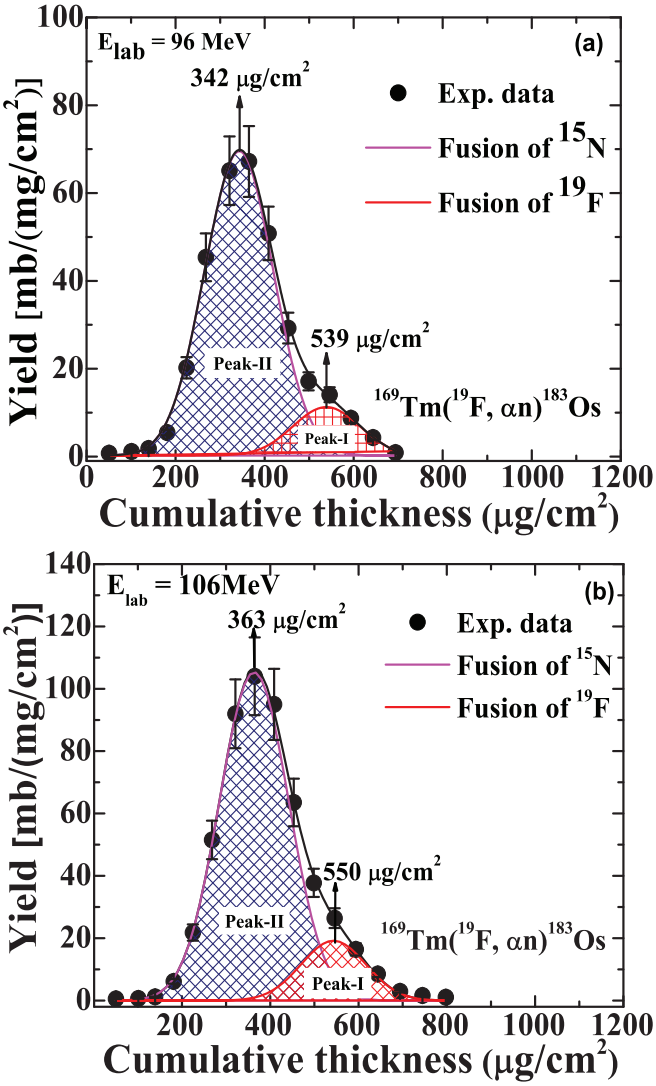


FIG. 6. [(a) and (b)] Experimentally measured recoil range distribution of $^{183}$Os residues populated through $\alpha$n channel in $^{19}F + ^{169}$Tm system at 96-MeV beam energy.

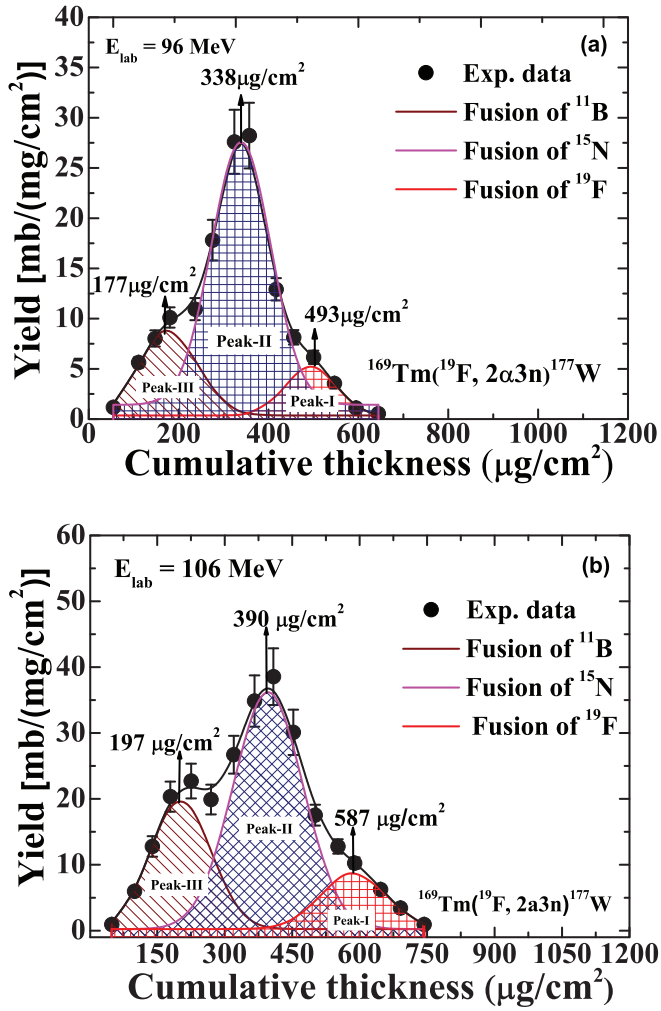


FIG. 7. [(a) and (b)] Experimentally measured recoil range distribution of $^{177}$W residues populated through $2\alpha 3n$ channel in $^{19}F + ^{169}$Tm system at energies 96 and 106 MeV.

the experimentally deduced ranges at both peaks indicates the presence of more than one LMT component. This suggests that the $^{183}$Os($\alpha n$) residues are also produced by another process involving a partial LMT component. The observation of two distinctly different momentum transfer events may be explained based on the breakup fusion model [56,57]. According to this model, when the $^{19}$F projectile approaches the target nucleus, it may break up into fragments, such as $^{19}F \rightarrow {}^{15}N + \alpha$. One of the fragments ($\alpha$) moves forward without interacting with the target nucleus, acting as a spectator, while the other fragment, $^{15}$N, fuses with the target nucleus, leading to the formation of an IFC system. This IFC system recoils in the forward direction, following momentum conservation. The theoretically calculated ranges using the SRIM code for the interaction of a $^{15}$N beam (ICF process) and a $^{19}$F beam (CF process) have been compared with the experimental ranges and found to be in good agreement, confirming the explanation mentioned above. Further, the $\rho_{LMT}$ for Peak-I is approximately 1, and for Peak-II is approximately 0.78. This confirms that both the ICF and CF processes contribute to the production of $^{183}$Os($\alpha n$) residues, with their respective contributions depending on the beam energy.

Similar observations have also been made for the $^{177}$W($2\alpha 3n$) residues, where the range distribution has been deconvoluted into three Gaussian peaks at different cumulative depths, as shown in Figs. 7(a) and 7(b). As can be seen from Fig. 7(a), the two peaks observed at lower cumulative depths, namely Peak-II and Peak-III, may be explained by assuming the break-up of the $^{19}$F projectile into $^{15}N + \alpha$ and/or $^{11}B + {}^{8}$Be. The experimentally deduced most probable ranges ($R^p_{exp}$) for $^{15}$N and $^{11}$B fusion are in good agreement with those estimated from SRIM calculations. The $R^p_{exp}$ for Peak-II and Peak-III obtained from the RRDs, are approximately 338 and 177 μg/cm$^2$, respectively, indicating the $^{15}$N fusion and $^{11}$B fusion with the $^{169}$Tm target. Similarly, Fig. 7(b) represents the range distribution of the same residues at energy 106 MeV showing three distinct peaks at different cumulative

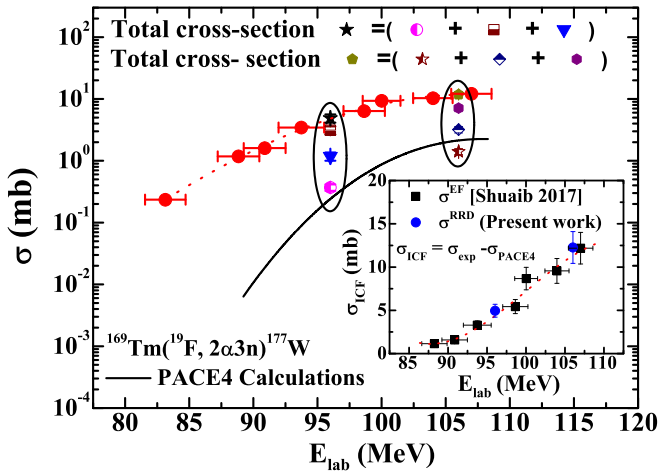


FIG. 8. A comparison between the cross sections in the measured EF of $^{177}$W($2\alpha 3n$) residues [25] and the corresponding values obtained from the range-integrated cross sections based on RRD measurements of the same residues produced in the $^{19}$F + $^{169}$Tm reaction. The solid black line represents the theoretical prediction of the PACE4 code, with the red dotted line provided as a visual guide. The inset figure compares the ICF cross sections derived from the RRD data with those deduced from the excitation function [25], showing the relationship as a function of the beam energy.

depths. The Peak-II and Peak-III corresponds to the fusion of $^{15}$N and $^{11}$B fragments of $^{19}$F with $^{169}$Tm target. Further, the experimentally measured cross section for the fusion of $^{11}$B is found to be lower than that for $^{15}$N fusion with the target. The break-up threshold for $\alpha + {}^{15}$N and $2\alpha + {}^{11}$B are respectively 4 and 15 MeV. In the present case, the experimentally measured cross section for $^{15}$N fusion (and one $\alpha$ emission) is found to be higher than $^{11}$B (and two $\alpha$ emission) as expected. The experimentally measured cross section for these two components at both studied energies is also found to be higher as compared to PACE4 code and is found to be in good agreement with the cross section measured in EF of $^{177}$W($2\alpha 3n$) residues (see Fig. 8). It may be pertinent to mention that there is no theoretical explanation available in the literature regarding the breakup of $^{19}$F into $^{11}$B + $^{8}$Be. The identification of $^{177}$W residues populated via the $2\alpha 3n$ channel has been confirmed both experimentally, through its characteristic $\gamma$ lines ($E_\gamma = 1036.4$ keV), and by its measured ranges in this study. The same residues were also identified through the characteristic $\gamma$-ray emissions of $^{177}$W ($t_{1/2} = 2.2$ h) within the same system [25]. In this study, the population of $^{177}$W residues has been identified based on their measured half-life, which reasonably aligns with the value documented in the literature. However, it might be intriguing to explore the theoretical aspects of the breakup of $^{19}$F into $^{11}$B + $^{8}$Be. The details of the experimentally deduced most probable ranges ($R^p_{\rm exp}$) along with the corresponding theoretical ranges ($R^p_{\rm theo}$) calculated by the SRIM code [50] at both incident energies are given in Tables III and IV. It is important to consider that particles emitted from the forward-moving recoiling products may influence the energy and momentum of the final residues within the stopping medium. These effects are reflected in the full width at half maximum (FWHM) of the experimentally derived recoil range distribution. Additionally, the width may also be influenced by contributions from straggling effects. To ensure consistency in the observed FWHM values of the recoil ranges for the evaporation residues, we calculated normalized FWHM values using the relation FWHM/$R^p_{\rm exp}$. These normalized FWHM values are presented in Table V of the paper. It can be observed from the table that the normalized FWHM values are consistent for both CF and ICF residues individually. In the case of CF channels with $\alpha$-emitting residues, the average peak resolution is around 0.35. However, for ICF-$\alpha$ and ICF-$2\alpha$ channels, the average peak resolution increases to about 0.50 and 1.13, respectively. This analysis helps us evaluate the consistency in the FWHM observed in the recoil ranges of the evaporation residues, offering insights into the resolution of the detected peaks. The variations in peak resolution between CF and ICF channels stem from the different dynamics and processes involved in each reaction pathway.

From the measured distributions (Figs. 5–7), the relative contributions of different reaction channels have been obtained by deducing the range-integrated cross sections ($\sigma^{\rm exp}_{\rm RIC}$)

TABLE III. Experimentally deduced most probable mean ranges ($R^{\rm exp}_p$) of all identified residues from the RRD figures and theoretically calculated ranges of all observed residues using SRIM code in Al in the units of μg/cm$^2$ for CF and ICF components in the interaction of $^{19}$F + $^{169}$Tm system at energy ≈96 MeV.

| Residues | $R^{\rm exp}_P$ (μg/cm$^2$) CF | $R^{\rm theo}_P$ (μg/cm$^2$) CF | $R^{\rm exp}_P$ (μg/cm$^2$) ICF-$\alpha$ | $R^{\rm theo}_P$ (μg/cm$^2$) ICF-$\alpha$ | $R^{\rm exp}_P$ (μg/cm$^2$) ICF-$2\alpha$ | $R^{\rm theo}_P$ ICF-$2\alpha$ |
|---|---|---|---|---|---|---|
| $^{184}$Pt($4n$) | 509 ± 34 | 513 | — | — | — | — |
| $^{183}$Pt($5n$) | 515 ± 33 | 513 | — | — | — | — |
| $^{184}$Ir($p3n$) | 510 ± 43 | 513 | — | — | — | — |
| $^{183}$Ir($p4n$) | 511 ± 34 | 513 | — | — | — | — |
| $^{183}$Os($\alpha n$) | 539 ± 23 | 513 | 342 ± 23 | 343 | — | — |
| $^{181}$Os($\alpha 3n$) | 526 ± 23 | 513 | 334 ± 22 | 343 | — | — |
| $^{179}$Os($\alpha 5n$) | 542 ± 31 | 513 | 340 ± 23 | 343 | — | — |
| $^{177}$W($2\alpha 3n$) | 493 ± 29 | 513 | 338 ± 28 | 343 | 177 ± 25 | 194 |
| $^{175}$Ta($2\alpha p4n$) | — | 513 | — | 343 | — | 194 |

TABLE IV. Experimentally deduced most probable mean ranges ($R_p^{exp}$) of all identified residues from the RRD figures and theoretically calculated ranges of all observed residues using SRIM code in Al in the units of μg/cm$^2$ for CF and ICF components in the interaction of $^{19}F + ^{169}Tm$ system at energy ≈106 MeV.

| Residues | $R_P^{exp}$ (μg/cm$^2$) CF | $R_P^{theo}$ (μg/cm$^2$) CF | $R_P^{exp}$ (μg/cm$^2$) ICF-$\alpha$ | $R_P^{theo}$ (μg/cm$^2$) ICF-$\alpha$ | $R_P^{exp}$ (μg/cm$^2$) ICF-2$\alpha$ | $R_P^{theo}$ ICF-2$\alpha$ |
|---|---|---|---|---|---|---|
| $^{184}$Pt($4n$) | 548 ± 37 | 564 | — | — | — | — |
| $^{183}$Pt($5n$) | 555 ± 33 | 564 | — | — | — | — |
| $^{184}$Ir($p3n$) | 559 ± 41 | 564 | — | — | — | — |
| $^{183}$Ir($p4n$) | 561 ± 38 | 564 | — | — | — | — |
| $^{183}$Os($\alpha n$) | 550 ± 25 | 564 | 363 ± 25 | 378 | — | — |
| $^{181}$Os($\alpha 3n$) | 554 ± 25 | 564 | 360 ± 22 | 378 | — | — |
| $^{179}$Os($\alpha 5n$) | 553 ± 23 | 564 | 368 ± 23 | 378 | — | — |
| $^{177}$W($2\alpha 3n$) | 587 ± 25 | 564 | 390 ± 25 | 378 | 197 ± 28 | 215 |
| $^{175}$Ta($2\alpha p4n$) | — | 564 | 403 ± 36 | 378 | 228 ± 33 | 215 |

and comparing them with those obtained from the statistical model PACE4 calculations [48]. The theoretical model code PACE4 is based on the Hauser–Feshbach theory of compound nucleus decay and employs statistical approach to compound nucleus de-excitation through a Monte Carlo procedure. The calculation of the CF cross sections has been conducted using the BASS model [58]. Transmission coefficients for neutrons and protons are derived using the optical model potentials formulated by Becchetti and Greenlees [59], while $\alpha$-particle emissions are evaluated using Satchler's optical model [60]. Within this code, the level density parameter a ($= A/K$) MeV$^{-1}$ holds significance, where $A$ represents the mass number of the nucleus and $K$ denotes a free parameter that can be adjusted to match experimental data. In this study, a value of $K = 10$ has been utilized to reproduce the theoretical cross section for the $^{19}F + ^{169}Tm$ system. A comprehensive elucidation of the code PACE4 can be found in Refs. [25,27].

As a representative case, for $^{184}$Pt($4n$) residues shown in Figs. 5(a) and 5(b), the range-integrated cross section ($\sigma_{RIC}^{exp}$) is found to be approximately 146.7 ± 2.1 mb, which is in good agreement with $\sigma^{PACE} = 145$ mb at $E_{lab} = 96$ MeV. Similarly, at $E_{lab} = 106$ MeV, the $\sigma_{RIC}^{exp}$ is ≈28.1 ± 0.1 mb, and is in good agreement with $\sigma^{PACE} = 24$ mb. Likewise, for other CF channels (i.e., $xn$ and $pxn$), the predictions of the PACE4 code [48] agree well with the experimental data, except for $\alpha$-emitting channels which exhibit more than one LMT component. In such cases, the contribution of individual fusion components has been obtained for the corresponding fusion component. It may be noted that the statistical model code PACE4 does not consider the ICF process, and hence, it does not provide a satisfactory representation of the experimental data for all the $\alpha$-emitting channels [25]. As an example, for the $^{183}$Os($\alpha n$) residues (shown in Fig. 6), the experimentally deduced $\sigma_{RIC}^{exp}$ is approximately 13.5 mb ± 0.3, while the PACE4 value is only 0.3 mb. The significant enhancement of the experimental cross section compared to the PACE4 prediction clearly indicates the presence of breakup fusion, which is supported by the RRD components involved in the production of $^{183}$Os($\alpha n$) residues. Similarly, for the $2\alpha 3n$ channel (shown in Fig. 7) at 96 MeV, the experimentally deduced $\sigma_{RIC}^{exp}$ is approximately 4.9 ± 0.6 mb, while PACE4 predicts $\sigma^{PACE} = 0.2$ mb. However, the CF prediction of PACE4 and the one obtained from the RRD matches well. It is worth mentioning that during the analysis, it has been observed that the residues $^{184}$Ir($p3n$) are strongly fed from their higher charge isobar (referred to as precursor) $^{184}$Pt($4n$) through $\beta^+$ emission. Therefore, the independent range-integrated cross section ($\sigma_{ind}^{RIC}$) of the residues $^{184}$Ir($p3n$) has been extracted from the cumulative cross section ($\sigma_{cum}$) using the successive radioactive decay formulations presented in Ref. [28], based on the standard Bateman equations [61]. The experimentally deduced independent production cross section of $^{184}$Ir($p3n$) residues agrees well with the estimation by the statistical model code PACE4 [48].

The $\sigma_{RIC}^{exp}$ values have been determined for the different fusion components observed in the population of $^{177}$W($2\alpha 3n$) residues (shown in Fig. 7). It has been observed that Peak-I corresponds to the full LMT from the projectile to the target nucleus, achieved via the CF process. This is supported by the agreement between the experimentally deduced mean range

TABLE V. A comparison of normalized FWHM of recoil range distributions.

| Residue | ≈96 (MeV) CF | ≈106 (MeV) CF | ≈96 (MeV) ICF-$\alpha$ | ≈106 (MeV) ICF-$\alpha$ | ≈96 (MeV) ICF-2$\alpha$ | ≈106 (MeV) ICF-2$\alpha$ |
|---|---|---|---|---|---|---|
| $^{184}$Pt($4n$) | 0.56 | 0.62 | — | — | — | — |
| $^{183}$Pt($5n$) | 0.58 | 0.70 | — | — | — | — |
| $^{184}$Ir($p3n$) | 0.75 | 0.72 | — | — | — | — |
| $^{183}$Ir($p4n$) | 0.58 | 0.65 | — | — | — | — |
| $^{183}$Os($\alpha n$) | 0.30 | 0.32 | 0.51 | 0.51 | — | — |
| $^{181}$Os($\alpha 3n$) | 0.32 | 0.28 | 0.54 | 0.55 | — | — |
| $^{179}$Os($\alpha 5n$) | 0.36 | 0.31 | 0.50 | 0.55 | — | — |
| $^{177}$W($2\alpha 3n$) | 0.30 | 0.30 | 0.45 | 0.44 | 0.70 | 0.82 |
| $^{175}$Ta($2\alpha p4n$) | — | — | — | — | — | 1.13 |

TABLE VI. Experimentally deduced range-integrated cross section ($\sigma^{\rm exp}_{\rm RRD}$) from the RRD curves and theoretically calculated cross section ($\sigma^{\rm PACE4}$) using code PACE4 of all identified residues at energies ≈96 and 106 MeV.

| | $E_{\rm lab}$ = 96 MeV | | $E_{\rm lab}$ = 106 MeV | |
|---|---|---|---|---|
| Residues | $\sigma^{\rm RRD}_{\rm exp}$ (mb) | $\sigma^{\rm PACE}$ (mb) | $\sigma^{\rm RRD}_{\rm exp}$ (mb) | $\sigma^{\rm PACE}$ (mb) |
| $^{184}$Pt($4n$) | 146.7 ± 2.1 | 145 | 28.1 ± 0.1 | 24 |
| $^{183}$Pt($5n$) | 289.7 ± 3.3 | 281 | 303.1 ± 1.9 | 305 |
| $^{184}$Ir($p3n$) | 13.4 ± 0.1 | 12.8 | 2.8 ± 0.04 | 2.7 |
| $^{183}$Ir($p4n$) | 32.4 ± 0.4 | 33.8 | 80.6 ± 0.7 | 70.8 |
| $^{183}$Os($\alpha n$) | 13.5 ± 0.3 | 0.3 | 20.7 ± 0.4 | 2.4 |
| $^{181}$Os($\alpha 3n$) | 98.3 ± 1.3 | 32.1 | 30.6 ± 0.8 | 9.3 |
| $^{179}$Os($\alpha 5n$) | 7.4 ± 0.2 | 0.1 | 63.7 ± 1.7 | 20.2 |
| $^{177}$W($2\alpha 3n$) | 4.9 ± 0.6 | 0.2 | 11.5 ± 1.3 | 2.1 |
| $^{175}$Ta($2\alpha p4n$) | — | — | 31.5 ± 0.4 | — |

($\sigma^{\rm exp}_{\rm RIC}$) and the theoretically calculated most probable range ($R^{\rm exp}_P$) obtained from the SRIM code. Similarly, the partial linear momentum components. viz., $^{15}$N and $^{11}$B are also found to be in good agreement with the theoretically estimated mean ranges reproduced by SRIM code. Figure 8 shows the comparison of EFs data of $^{177}$W($2\alpha 3n$) residues [25] with the range-integrated cross section ($\sigma^{\rm exp}_{\rm RIC}$) obtained from the RRDs of the same residues populated via different fusion components. The contribution of different fusion components has been obtained by dividing the area under the peak of the corresponding fusion component by the total area associated with the experimental data. As can be observed from Fig. 8, the total $\sigma^{\rm exp}_{\rm RIC}$ (represented by black stars) is the sum of all fusion components (i.e., Peaks-I + Peak-II + Peak-III) is found to be higher as compared to the PACE4 calculations for the same set of parameters given in Ref. [25] and also are in good agreement with the experimentally measured EFs at $E_{\rm lab}$ ≈ 96 and 106 MeV. Additionally, in the inset of Fig. 8, the contribution of ICF has been deduced based on the range-integrated cross section from the measured RRD peaks due to breakup fusion components [27]. The results are then plotted as a function of the incident energy of the projectile. As anticipated, the contribution of ICF demonstrates a pronounced reliance on the energy of the projectile. The details of the range-integrated cross sections of all identified residues, along with PACE4 calculations at both energies, are tabulated in Table VI.

Figure 9 presents a comparison between the energy-dependent ICF fraction obtained from the measured RRD data and that deduced from EFs measurements. The breakup fusion fraction ($F_{\rm ICF}$) was determined by subtracting the range-integrated cross section ($\sigma^{\rm exp}_{\rm RIC}$) of the measured CF channels from the total cross sections ($\sigma_{\rm TF}$). The total fusion cross section ($\sigma_{\rm TF}$) is the sum of the CF cross section ($\sigma_{\rm CF}$) and the ICF cross section ($\sigma_{\rm ICF}$). The $\sigma_{\rm ICF}$ was derived by subtracting the observed ICF contribution from the predicted CF channels obtained using the PACE4 code, specifically $\sigma_{\rm ICF} = \sigma^{\alpha's}_{\rm exp} - \sigma^{\rm theo}_{\rm PACE}$ [27]. It's rather crucial to note that some excited residues could not be directly measured due to their

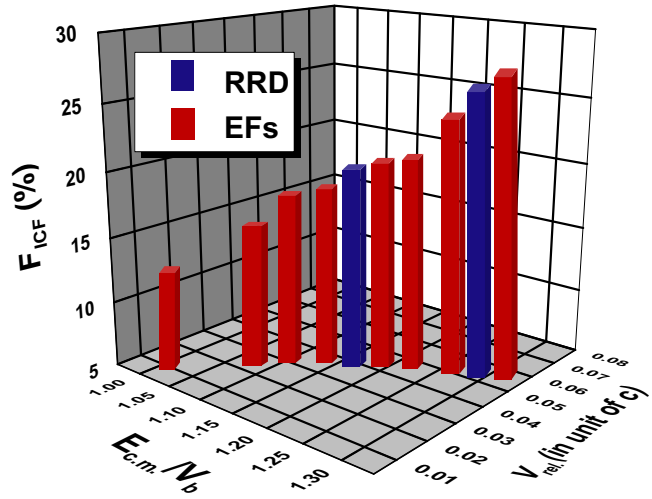


FIG. 9. A comparison of ICF fraction ($F_{\rm ICF}$) extracted from the analysis of RRDs (shown by blue vertical bars) and plotted as a function of normalized beam energy ($E_{\rm c.m.}/V_b$) and relative velocity ($v_{\rm rel}$). Data shown by red vertical bars indicates the percentage ICF fraction deduced from the analysis of EFs for the residues populated via CF and/or ICF in $^{19}$F + $^{169}$Tm (see text for more details).

shorter half-lives or weak intensity $\gamma$ lines. In order to have a comprehensive understanding of the dynamics in the breakup fusion/ICF process, the cross sections of these missing channels were incorporated using the statistical model code PACE4 [48].

## IV. SUMMARY AND CONCLUSIONS

In the present work, in order to study the reaction dynamics, the RRD of nine radionuclides, viz., $^{184}$Pt($4n$), $^{183}$Pt($5n$), $^{184}$Ir($p3n$), $^{183}$Ir($p4n$), $^{183}$Os($\alpha n$), $^{181}$Os($\alpha 3n$), $^{179}$Os($\alpha 5n$), $^{177}$W($2\alpha 3n$), and $^{175}$Ta($2\alpha p4n$) produced through fusion and/or breakup fusion processes, are measured at two distinct energies (≈96 and 106 MeV). The RRDs for $xn$ and $pxn$ channels show up a single Gaussian peak at both energies studied. Experimentally obtained range-integrated cross sections ($\sigma^{\rm exp}_{\rm RIC}$) for the fusion ($xn/pxn$) channels were found to be in good agreement with the predictions of the PACE4 code. This indicated that these residues were primarily formed due to complete momentum transfer from the projectile to the target nucleus. However, the RRDs of residues involving $\alpha$ particles in the exit channels exhibited multiple Gaussian peaks, suggesting the presence of both full and partial LMT events. These components were likely a result of the fusion of $^{15}$N and/or $^{11}$B fragments of $^{19}$F, in cases where $^{19}$F breaks up into $^{15}$N + $\alpha$ and/or $^{11}$B + $^{8}$Be. Additionally, the measured range-integrated cross section ($\sigma^{\rm exp}_{\rm RIC}$) for $\alpha$-emitting channels was notably higher than the statistical model predictions of the PACE4 code. Since the PACE4 code does not account for breakup reactions, this enhancement was attributed to partial fusion of the projectile, leading to the population of the same residues formed via the complete fusion process. This suggested the involvement of both full and partial LMT, particularly the $^{15}$N and

$^{11}B$ components. The different fusion components resulting from $^{15}N$ and $^{11}B$ fusion were confirmed based on the measured ranges of $\alpha$-emitting channels, which were in agreement with the predicted mean ranges obtained using the SRIM code.

Therefore, the study successfully represents the reliability and validity of the measurement techniques utilized by effectively differentiating between CF and ICF events through a self-consistent approach. The comprehensive examination of the recoil range distribution provides convincing evidence of break-up fusion in HI collisions at low energies. This clearly elucidates the significance of both complete and partial momentum transfer, as well as the fusion of $^{15}N$ and $^{11}B$ fragments in addition to the fusion of the $^{19}F$ projectile itself. The relative contribution of breakup and fusion components were observed to depend on energy.

## ACKNOWLEDGMENTS

The authors extend their gratitude to the Chairperson of the Department of Physics at Aligarh Muslim University, Aligarh, and the Director of IUAC, New Delhi, for generously providing all the essential facilities to conduct this research. M.S.A. and B.P.S. acknowledge the DST-SERB for their financial support through Project No. CRG/2020/000136. Special thanks are also extended to the Department of Physics at IIT Ropar, India, for providing the HPGe detector for the experiments.

[1] A. C. Berriman *et al.*, Nature (London) **413**, 144 (2001).
[2] S. Hofmann *et al.*, Eur. Phys. J. A **32**, 251 (2007); **14**, 147 (2002).
[3] R. N. Sagaidak, M. L. Chelnokov, V. I. Chepigin, V. A. Gorshkov, O. N. Malyshev, A. G. Popeko, A. I. Svirikhin, and A. V. Yeremin, Phys. Rev. C **105**, 024604 (2022).
[4] V. I. Zagrebaev, Nucl. Phys. A **734**, 164 (2004).
[5] B. B. Back, H. Esbensen, C. L. Jiang, and K. E. Rehm, Rev. Mod. Phys. **86**, 317 (2014).
[6] L. Corradi *et al.*, Nucl. Phys. A **734**, 237 (2004).
[7] Y. T. Oganessian *et al.*, Nature (London) **400**, 242 (1999).
[8] R. Bock *et al.*, Nucl. Phys. A **388**, 334 (1982).
[9] J. Tōke *et al.*, Nucl. Phys. A **440**, 327 (1985).
[10] W. Q. Shen *et al.*, Phys. Rev. C **36**, 115 (1987).
[11] M. G. Itkis *et al.*, Int. J. Mod. Phys. E **16**, 957 (2007).
[12] M. Dasgupta *et al.*, Phys. Rev. C **70**, 024606 (2004).
[13] C. S. Palshetkar *et al.*, Phys. Rev. C **89**, 024607 (2014).
[14] L. S. Gasques, D. J. Hinde, M. Dasgupta, A. Mukherjee, and R. G. Thomas, Phys. Rev. C **79**, 034605 (2009).
[15] L. F. Canto, R. Donangelo, L. M. deMatos, M. S. Hussein, and P. Lotti, Phys. Rev. C **58**, 1107 (1998).
[16] L. F. Canto *et al.*, Nucl. Phys. A **821**, 51 (2009).
[17] P. R. S. Gomes *et al.*, Nucl. Phys. A **834**, 151c (2010).
[18] L. F. Canto *et al.*, J. Phys. G: Nucl. Part. Phys. **36**, 015109 (2009).
[19] I. M. Bhat *et al.*, Nucl. Phys. A **1021**, 122421 (2022).
[20] B. Wang, W. J. Zhao, P. R. S. Gomes, E. G. Zhao, and S. G. Zhou, Phys. Rev. C **90**, 034612 (2014).
[21] M. Shuaib *et al.*, Phys. Rev. C **98**, 014605 (2018).
[22] M. S. Asnain, M. Shuaib, I. Majeed, M. K. Sharma, V. R. Sharma, A. Yadav, D. P. Singh, P. P. Singh, S. Kumar, R. Kumar, B. P. Singh, and R. Prasad, Phys. Rev. C **105**, 014609 (2022).
[23] M. Shuaib *et al.*, JPS Conf. Proc. **32**, 010015 (2020).
[24] M. S. Asnain, M. Shuaib, I. Majeed, M. K. Sharma, V. R. Sharma, A. Yadav, D. P. Singh, P. P. Singh, U. Gupta, R. N. Sahoo, A. Sood, M. Kaushik, S. Kumar, R. Kumar, B. P. Singh, and R. Prasad, Phys. Rev. C **104**, 034616 (2021).
[25] M. Shuaib *et al.*, J. Phys. G: Nucl. Part. Phys. **44**, 105108 (2017).
[26] M. S. Asnain *et al.*, Phys. Rev. C **106**, 064607 (2022).
[27] A. Yadav *et al.*, Phys. Rev. C **107**, 044605 (2023).
[28] M. Cavinato, E. Fabrici, E. Gadioli, E. G. Erba, P. Vergani, M. Crippa, G. Colombo, I. Redaelli, and M. Ripamonti, Phys. Rev. C **52**, 2577 (1995).
[29] P. Vergani, E. Gadioli, E. Vaciago, E. Fabrici, E. G. Erba, M. Galmarini, G. Ciavola, and C. Marchetta, Phys. Rev. C **48**, 1815 (1993).
[30] D. J. Parker, J. J. Hogan, and J. Asher, Phys. Rev. C **35**, 161 (1987).
[31] J. Wilczynski *et al.*, Nucl. Phys. A **373**, 109 (1982).
[32] K. Siwek-Wilczynska, E. H. du Marchie van Voorthuysen, J. van Popta, R. H. Siemssen, and J. Wilczynski, Phys. Rev. Lett. **42**, 1599 (1979).
[33] P. E. Hodgson, *Introductory Nuclear Physics* (Oxford University Press, Oxford, 2003).
[34] E. Takada, T. Shimoda, N. Takahashi, T. Yamaya, K. Nagatani, T. Udagawa, and T. Tamura, Phys. Rev. C **23**, 772 (1981).
[35] J. P. Bondorf *et al.*, Nucl. Phys. A **333**, 285 (1980).
[36] A. Yadav *et al.*, Phys. Rev. C **85**, 064617 (2012).
[37] D. J. Parker, J. Asher, T. W. Conlon, and I. Naqib, Phys. Rev. C **30**, 143 (1984).
[38] A. Diaz-Torres, D. J. Hinde, J. A. Tostevin, M. Dasgupta, and L. R. Gasques, Phys. Rev. Lett. **98**, 152701 (2007)
[39] P. Singh *et al.*, Phys. Rev. C **80**, 064603 (2009); **78**, 017602 (2008).
[40] A. Yadav *et al.*, Phys. Rev. C **85**, 034614 (2012).
[41] M. K. Sharma, Unnati, B. K. Sharma, B. P. Singh, H. D. Bhardwaj, R. Kumar, K. Golda, and R. Prasad, Phys. Rev. C **70**, 044606 (2004).
[42] D. Sing *et al.*, AIP Conf. Proc. **1609**, 39 (2014).
[43] R. Otani, R. Kageyama, M. Iwasaki, M. Kudo, M. Tomita, and M. Ito, Phys. Rev. C **90**, 034316 (2014).
[44] M. La Cognata *et al.*, Phys. Rev. C **99**, 034301 (2019).
[45] F. Nemoto and H. Bando, Prog. Theor. Phys. **47**, 1210 (1972).
[46] T. Sakuda and F. Nemoto, Prog. Theor. Phys. **62**, 1274 (1979).
[47] S. Wilmes, V. Wilmes, G. Staudt, P. Mohr, and J. W. Hammer, Phys. Rev. C **66**, 065802 (2002).
[48] A. Gavron, Phys. Rev. C **21**, 230 (1980).
[49] N. G. Puttaswamy *et al.*, *DAE Symposium on Nuclear Physics, Bombay, 1991*, Vol. 34B (DAE, Mumbai, 1991).
[50] The Stopping and Range of Ion Matter (SRIM) [http://www.srim.org/SRIM/SRIMLEGL.htm].
[51] E. T. Subramaniam, K. Rani, B. P. Ajith Kumar, and R. K. Bhowmik, Rev. Sci. Instrum. **77**, 096102 (2006).

[52] E. Browne and R. B. Firestone, *1996 Table of Radioactive Isotopes* (Wiley, New York, 1996).
[53] J. K. Tuli, *2000 Nuclear Wallet Card, National Nuclear Data Centre* (Brookhaven National Laboratory, Brookhaven, NY, 2000).
[54] W. R. Leo, *Techniques for Nuclear an Particle Physics Experiments* (Springer, Berlin, 2010).
[55] ORIGIN, Lab-data analysis and graphing software [http://www.originlab.com/].
[56] J. R. Wu and I. Y. Lee, Phys. Rev. Lett. **45**, 8 (1980).
[57] T. Udagawa and T. Tamura, Phys. Rev. Lett. **45**, 1311 (1980).
[58] R. Bass, Nucl. Phys. A **231**, 45 (1974).
[59] F. D. Becchetti and G. W. Greenlees, Phys. Rev. **182**, 1190 (1969).
[60] G. R. Satchler, Nucl. Phys. **70**, 177 (1965)
[61] R. D. Evans, *The Atomic Nucleus* (McGraw–Hill, New York, 1955).

*Correction:* The byline footnote for author R. Kumar was missing at publication and has been inserted.